APPLIED PHYSICS

Stretchable broadband photo-sensor sheets for nonsampling, source-free, and label-free chemical monitoring by simple deformable wrapping

Kou Li[1,2]†, Teppei Araki[3]†, Ryogo Utaki[1,2], Yu Tokumoto[1,2], Meiling Sun[1,2], Satsuki Yasui[1,2], Naoko Kurihira[3], Yuko Kasai[3], Daichi Suzuki[4], Ruben Marteijn[5], Jaap M.J. den Toonder[5], Tsuyoshi Sekitani[3]*, Yukio Kawano[1,2,6,7]*

Chemical monitoring communicates diverse environmental information from industrial and biological processes. However, promising and sustainable systems and associated inspection devices that dynamically enable on-site quality monitoring of target chemicals confined inside transformable and opaque channels are yet to be investigated. This paper designs stretchable photo-sensor patch sheets for nonsampling, source-free, and label-free on-site dynamic chemical monitoring of liquids flowing inside soft tubes via simple deformable surface wrapping. The device integrates carbon nanotube–based broadband photo-absorbent thin films with multilayer-laminated stretchable electrodes and substrates. The patterned rigid-soft structure of the proposed device provides durability and optical stability against mechanical deformations with a stretchability range of 70 to 280%, enabling shape-conformable attachments to transformable objects. The effective use of omnidirectional and transparent blackbody radiation from free-form targets themselves allows compact measurement configuration and enhances the functionality and simplicity of this scheme, while the presenting technology monitors concentrations of arbitrary water-soluble chemicals.

INTRODUCTION

Chemical monitoring continuously collects diverse environmental information (1) and can anticipate future events based on changes in the obtained signals (2). Abnormality inspections in industrial equipment (3, 4), wastewater treatment (5), and food or beverage productions (6, 7) have been performed by involving the quantitative evaluation of specific chemicals or identifying contaminants. Biofluid monitoring also facilitates a variety of applications (8–10). To enrich these potentials, promising monitoring methods should be developed. In particular, nonsampling and label-free configurations for on-site chemical testing and transparency against containers and stretchability for adapting dynamic conditions of even opaque transformable packaging are all essential on monitoring systems and devices.

Numerous chemical monitoring strategies include centrifugation measurements (11), reagent reaction observations (12), biomarker tests (13), and secrete biofluid monitoring (14). However, these schemes require invasive sampling or labeling of chemicals, thus

hindering target-friendly operations. The above methods statically function where targets are examined within testing device packaging, rather than natural behaviors, being a bottleneck toward practical on-site use. To eliminate these disadvantages, photo-sensing techniques that do not require sampling and enable label-free chemical monitoring have been developed. Some well-established methods include ultraviolet (UV) or visible-light fluorescence (15) and absorbance (16) measurements for organic pollutant detection, oil content sensing, and carcinogenic polycyclic aromatic hydrocarbon testing. However, despite their nonsampling and label-free characteristics, the low transparency of UV–visible-light irradiation in opaque containers such as plastic and silicon makes nondestructive inspections difficult. Therefore, terahertz (THz) and infrared (IR) blackbody radiation (BBR) based on Planck's law from chemicals themselves should be effectively used for nonsampling and label-free monitoring of the targets inside opaque flow channels. Chemicals often exist in a dissolved state in liquids, and liquid samples generally absorb THz and IR irradiation (17), hindering opportunities for their fundamental transmissive or reflective photo-sensing measurements because of signal shortage. On the other hand, passive sensing associated with BBR, where the targets themselves behave as photo-sources, can mitigate the aforementioned limitation. Simultaneously, BBR-based passive THz-IR chemical monitoring permits compact measurement systems without the need for external photo-sources and associated optical systems.

To this end, operations under broad THz-IR radiation at room temperature and mechanically stretchable device configurations are essential for photo-detectors. Broadband operation facilitates the effective detection of BBR across wide frequency bands. Uncooled photo-sensing systems, which are free from bulky cooling equipment, are indispensable for mobile use. Bolometers (18) and other solid-state semiconductor photo-detectors (19) allow uncooled broadband THz-IR detection. However, their rigid unbendable

[1]Laboratory for Future Interdisciplinary Research of Science and Technology, Tokyo Institute of Technology, 2-12-1 Ookayama, Meguro-ku, Tokyo 152-8552, Japan. [2]Department of Electrical and Electronic Engineering, School of Engineering, Tokyo Institute of Technology, 2-12-1 Ookayama, Meguro-ku, Tokyo 152-8552, Japan. [3]The Institute of Scientific and Industrial Research, Osaka University, 8-1 Mihogaoka, Ibaraki-shi, Osaka 567-0047, Japan. [4]Sensing System Research Center, National Institute of Advanced Science and Technology, 807-1 Shuku-machi, Tosu-shi, Saga 841-0052, Japan. [5]Department of Mechanical Engineering and Institute for Complex Molecular Systems, Eindhoven University of Technology, Eindhoven 5600 MB, Netherlands. [6]Department of Electrical, Electronic, and Communication Engineering, Faculty of Science and Engineering, Chuo University, 1-13-27 Kasuga, Bunkyo-ku, Tokyo 112-8551, Japan. [7]National Institute of Informatics, 2-1-2 Hitotsubashi, Chiyoda-ku, Tokyo 101-8430, Japan.
*Corresponding author. Email: sekitani@sanken.osaka-u.ac.jp (T.S.); kawano@elect.chuo-u.ac.jp (Y.Kaw.)
†These authors contributed equally to this work.

structures restrict measurement configurations such as the shape and size of liquid flow channels and containers. Three-dimensional (3D) curvilinear cylinders often used for liquid flow channels present blind areas for rigid sensors, degrading the measurement accuracy. On the other hand, flexible uncooled broadband THz-IR detectors can be attached to arbitrarily structured outer surfaces (20). The flexible detector therefore enables omnidirectional BBR detection of 3D objects such as a spirally wrapped heat pipe (21) and a man's hand (22). Moreover, mechanically stretchable photo-detectors are suitable for transformable soft outer surfaces that are dynamically modulated by inherent liquid fluidity, including medical rubber tubes and bellow hoses. Nevertheless, stretchable uncooled broadband THz-IR detectors have yet to be fully designed and implemented, and corresponding BBR-based on-site dynamic monitoring of in-liquid chemicals has not been presented as well.

Here, this paper designs stretchable and freely deformable broadband photo-sensor patch sheets (Fig. 1, A and B) and demonstrates nondestructive and nonsampling, photo-source–free, and label-free passive on-site dynamic monitoring of in-liquid chemical substances by simply wrapping the outer surface of the fluid channel (Fig. 1C). The sensor channel consists of carbon nanotube (CNT) network–based photo-thermoelectric (PTE) thin films and is well capable of uncooled broadband THz-IR detection. The device integrates CNT film channels with multilayer-laminated stretchable electrodes and substrates. A rigid-soft pattern on the device prevents the channel from strain-induced distortion and ensures durability and optical stability against mechanical deformations under a whole device strain range of 70 to 280%. This approach allows BBR-based monitoring schemes involving photo-induced deformation detection of balloons and 360° around-view imaging of concealed 3D liquid flowing inside opaque columns around which the patch sheet is firmly wrapped without bulky rotation stages. This results in nondestructive and nonsampling, photo-source–free, label-free, and passive on-site dynamic concentration monitoring of in-liquid chemicals (Table 1). The approach presented also advantageously monitors concentrations of arbitrary water-soluble chemicals by detecting changes in BBR signals from solvents before and after chemical dissolution. The versatility of low-cost device printing methods and the simplicity of measurements that only require patching the sheet on arbitrary containers can help develop mobile easy-to-operate chemical quality assessment platforms available to anyone, not just experts. Potential applications include beverage and food quality monitoring. The proposed patch sheets can be wrapped outside containers and coating for sugar content or temperature monitoring based on the inherent BBR of the targets, while external THz-IR irradiation can be applied for impurity detection such as water pipes or beverage can inspections (20), simultaneously.
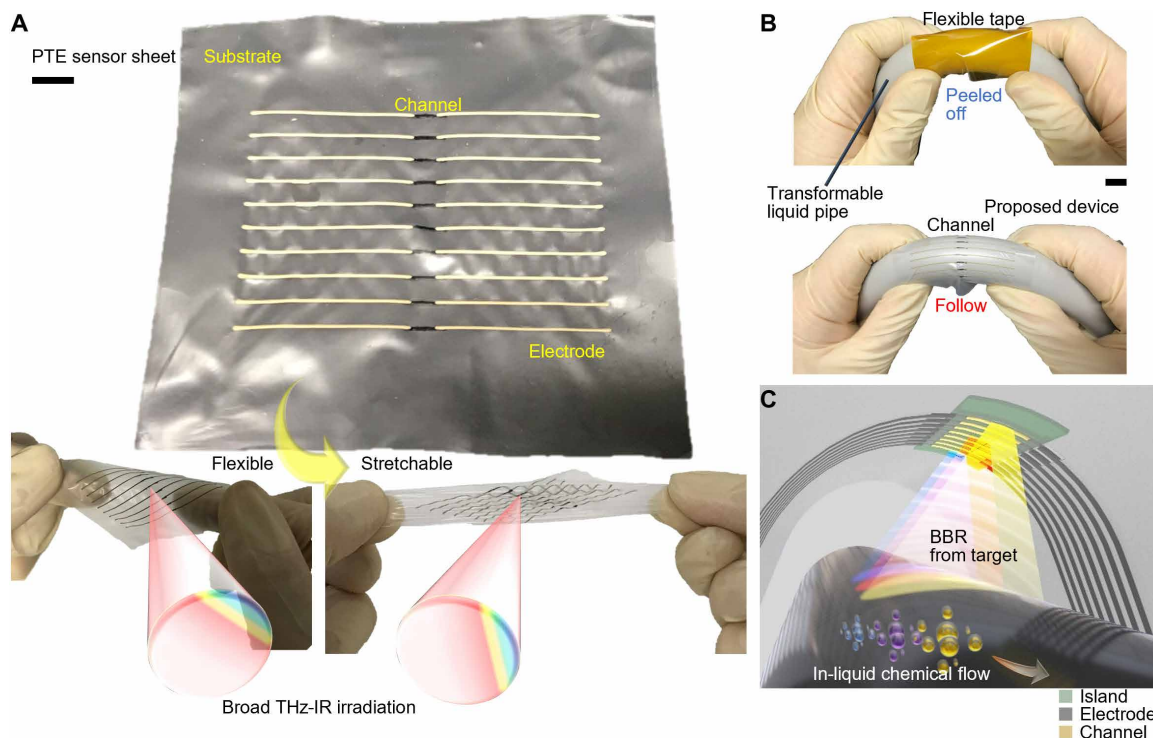

Fig. 1. Conceptual diagram of this work. (**A**) Photographs of the stretchable broadband photo-sensor array sheet. The sheet consists of a flexible CNT film PTE channel, elastic readout electrodes, and a PU film substrate (figs. S1 to S4). Scale bar, 3 mm. (**B**) Simple comparison of mechanical followability between a versatile flexible tape and the stretchable PTE sensor sheet against movements of a 3D object. Rubber liquid tubes are wrapped with the flexible tape and the stretchable scanner sheet. Both wrapping configurations allow multiview monitoring. On the other hand, the stretchable sheet device wrapping advantageously follows the bending of the tube, while the flexible tape is easily peeled off from the tube. This means that the stretchable scanner sheet wrapping configuration enables on-site monitoring of even soft moveable target objects. Scale bar, 5 mm. (**C**) Scheme of the nondestructive and nonsampling, source- and label-free, passive, and on-site dynamic in-liquid chemical photo-monitoring by the simple outer surface wrapping. The proposed device is firmly attached to curvilinear liquid transport objects to comprehend the inner solution concentration by BBR signal scanning.

Table 1. Potential functionality comparison of the demonstrated concept in this work with standard in-liquid chemical testing methods.

Method	Sample	Label	Transparency	Photo-source
This work	No need*	No need	◎†	No need
UV absorption	No need	No need	△‡	Need
UV fluorescence	No need	No need	△‡	Need
Centrifugation	Need	No need		
Reagent reaction	No need	Need		
Biomarker	Need	Need		
Secretory fluid	Need	No need		

*Available for solution concentration monitoring with a single solute by the technology presented here. †Transparent to nonmetallic opaque containers. ‡Transparent to visible containers.

RESULTS

Fundamental device design for a stretchable PTE sensor sheet

Figures S1 (A to D), S2, S3 (A and B), and S4 (A to D) first discuss the basics behind the stretchable broadband PTE sensor sheet (Fig. 2A), including the operating principle, fabrication process, thermal durability and corresponding optical stability, and fundamental device structure. The PTE effect governs uncooled broadband photo-detection (fig. S1A). The photo-induced heating and associated thermal distribution across CNT film channels trigger the Seebeck effect. The channel consists of a PN junction as a photo-detection interface at the center position (fig. S1B). The liquid coating with an N-type chemical carrier dopant on a half-side of originally P-type CNT films brings local transition of the positive Seebeck coefficients into negative values (fig. S1C; also see the "Chemical carrier doping" section in Materials and Methods), maximizing the PTE response (fig. S1D). A 1-μm-thick flexible CNT thin-film photo-absorber, consisting of randomly stacked and semiconducting metallic-mixed single-walled CNTs (SWCNTs), has served as channel materials for freely bendable broadband photo-detectors (22). In this study, the CNT film channel was embedded in a stretchable device framework: a supporting substrate and a readout electrode. A polyurethane (PU) film with a thickness of 8 μm would serve as a sealing layer of the channel, and fig. S2 assures the optical suitability of the PU sealing based on its high transparency in broad THz and IR regions. Figure S3 (A and B) presents the device fabrication process, and selective suction CNT film patterning and inkjet electrode printing allow for flexible design of fundamental device characteristics (e.g., size, shape, pitch, and element number). Selective suction CNT film patterning and stretchable PTE sensor sheet design in Materials and Methods respectively describe the corresponding experimental details. The thermal durability and associated optical stability of CNT film channels were investigated to assure stretchable device packaging that requires periodic annealing steps (electrode baking and multilayer lamination) up to 100°C. Figure S4 (A to D) maps photo-responses of the PN junction–type CNT film PTE sensor for different device annealing temperatures. The results present sufficient photo-response stability that was maintained with device annealing up to 200°C. Although the thermal durability and corresponding optical stability of the wet-processed chemical carrier doping on SWCNT films (23) used here were previously unclear, the above assessment proved that embedding doped channels in the proposed device design is available. A partially patterned epoxy resin on the rear surface of the PU substrate (figs. S5 and S6), whose location corresponds to that of the channel on the front side (Fig. 2, B and C), serves as a rigid stiffener. Such partial rigid-soft patterning technique typically handles mounting of light-emitting diodes (LEDs) on PU substrates (24) and so on and is even suitable for the above PTE sensor coupling. Figure 2D presents a finite element method (FEM) simulation of strain distribution on the stretched PU substrate with the partial epoxy stiffener, indicating that the distortion-free behavior was maintained on the stiffened region.

Figure 2E then statistically presents electrical resistance change behaviors via device stretching to understand the electrical stability against mechanical deformations. The change in electrode resistance ($\Delta R/R_0$) exhibits degradation up to over 10 to 120 times increment against 50% strain (fig. S7), where ΔR and R_0 correspond to the fluctuation and initial value of electrical resistance. Meanwhile, the obtained result indicates that the change in device resistance was suppressed to 6% increment against 50% strain. The aforementioned partial rigid-soft patterning contributes to the presented electrical stability of the device. The resistance of the CNT film channel dominantly accounts for the total device resistance, and the initial resistance values of the electrode and channel are approximately sub–1 ohm and 1 kilohm, respectively. As mentioned earlier, the epoxy stiffener beneath the channel maintains the distortion-free state of CNT films, thus avoiding the associated significant change in device resistance (25, 26). The epoxy resin stiffener on the PU substrate did not peel off and maintained adhesion strength even during 100 cycles of repeated stretching between 0 and 100% strain and subsequent adhesive tape peel testing. Figures S7 to S9 indicate that the use of multilayered PU substrate films potentially reduces the degradation of electrode resistance against stretching. Figure 2F further demonstrates an influence of the rigid-soft patterning for the change in device resistance against stretching. The sudden increments of resistance values in the graph correspond to device breakages. The obtained result indicates that the rigid-soft patterning provides higher stretchability (70% strain) for the device compared to that of the unstiffened one (10% strain). Here, fig. S10 (A and B) depicts that the device breakage occurred at a stiffener boundary of the proposed device and at the channel-electrode junction for the unstiffened one.
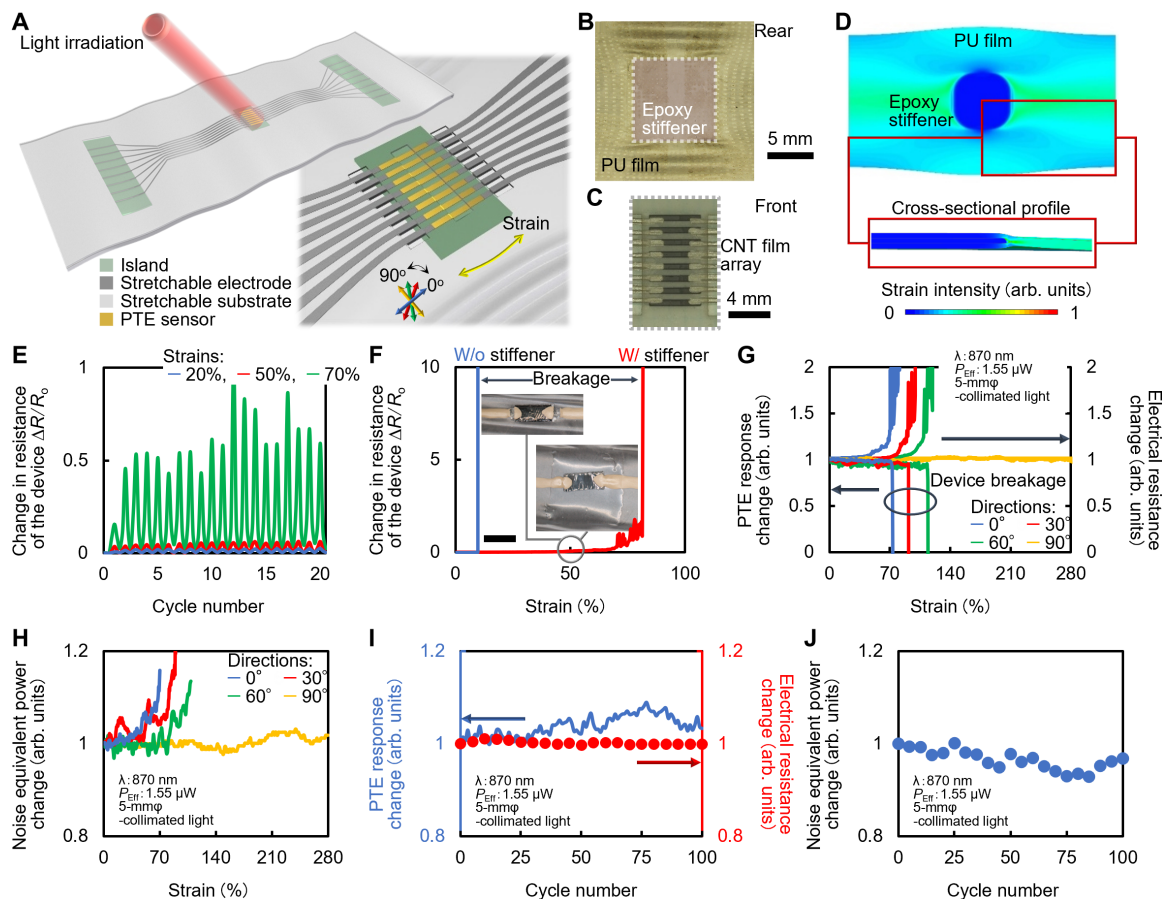
Fig. 2. Durability and optical stability of the stretchable PTE sensor sheet against mechanical deformations. (**A**) Schematic of the proposed device. (**B**) Rigid-soft patterning on a PU substrate. FEM simulation of strain distribution represents that (**C**) a partial epoxy stiffener provides (**D**) a distortion-free state of the channels. (**E**) Changes in device resistance values against 20 to 70% strains. (**F**) Changes in resistance values of devices with and without the stiffener against stretching. The evaluated devices commonly equip the PU substrate, the transferred channel, and the elastic electrodes. Scale bar, 2 mm. (**G**) Changes in PTE responses of the device under external NIR ($\lambda = 870$ nm) irradiation and device resistance values against omnidirectional stretching. The observed changes in both signals clarified the stability of (**H**) the photo-detection sensitivity of the device against omnidirectional stretching. (**I**) Changes in PTE responses of the device under external NIR irradiation and device resistance values against repetitive stretching (50% strain in 0° direction). The evaluated devices consist of the PU substrate, the epoxy stiffener, the transferred channel, and the elastic electrodes (E, G, and I). The observed changes in both signals clarified the stability of (**J**) the NEP values of the device against repetitive stretching.

Regarding the optical characteristics of the device against mechanical deformations, Fig. 2G maps changes in PTE responses and resistance with omnidirectional stretching. The obtained result advantageously exhibits strain-independent photo-response behaviors before device breakages. Here, the device operation mechanism of the PTE effect (fig. S1A) and the aforementioned electrical stability of the proposed device facilitate this unique phenomenon. The change in device resistance governs the noise voltage in photo-responses, and the signal intensity of photo-responses is attributed to the effective Seebeck coefficient at the photo-detection interface and photo-induced thermal gradient across the channel. Owing to the zero-bias voltage operation of CNT film PTE sensors (*27*), the device noise voltage can be approximated to the theoretical lower limit of the thermal noise (the "Noise equivalent power evaluation" section in Materials and Methods describes the corresponding details). While the intensity of noise voltages is proportional to R^{-1}, the device noise was suppressed to several tens of nanovolts even for stretched configurations, as shown in fig. S10C. Here, the presented

suppression of the change in device resistance against strains with the rigid-soft patterning leads to the above noise management. The CNT film PTE sensor typically exhibits photo-response voltage signals ranging from hundreds of microvolts to a few millivolts (*20*), and the aforementioned device design strategy relaxes the mechanical deformation–induced degradation of photo-responses. Meanwhile, the device breakage caused failures of PTE responses (sudden signal reduction in Fig. 2G). Since the CNT film PTE sensor detects changes in the open-circuit voltage as photo-responses, the device breakage and disconnection induce loss of detection signals. For the angle dependence of device stretchability (positions for the sudden PTE signal reduction in the horizontal axis of Fig. 2G), the effective tension strain along the channel and electrode direction is thought to govern the fundamental characteristics. The effective tension strain along the device length direction can be estimated by the cosine component of the applied force as shown in fig. S11A. Among stretching directions from 0° to 90°, the larger the angle becomes, the weaker the effective tension strain along the device length

direction becomes. Relatedly, the device exhibits higher stretchability for larger stretching angles, as shown in fig. S11B. As the stretching direction approaches 90°, a compressive force is applied to the electrode. Against the buckling and wrinkling that occur in the thin-film substrate due to compression, the resistance fluctuation of the electrode is small. As a result, the electrode resistance does not affect the device performance and contributed to the stable photo-response up to 280% strain.

Figure 2H finally evaluates the optical stability of the device against mechanical deformations, from the viewpoint of changes in the noise equivalent power (NEP), which was used in a photo-detection sensitivity index for the CNT film PTE sensor. As NEP values are proportional to $R^{1/2}\Delta V^{-1}$ (ΔV: photo-response voltage signals; the "Noise equivalent power evaluation" section in Materials and Methods describes the corresponding details), the obtained distribution of each parameter in Fig. 2G clarified the change in NEP values. The graph indicates the change in NEP values of the device before device breakage was suppressed to at most 20% degradation against omnidirectional stretching. Regarding the device durability, Fig. 2I maps changes in PTE responses and resistance of the device against repetitive stretching (50%) up to 100 cycles. Figure 2J further evaluates the NEP stability against the above deformations and infers changes in photo-detection sensitivities that were suppressed within 10%. To sum up these, the proposed device exhibits stability and durability in terms of the photo-detection sensitivity as follows: inherent flexibility including CNT film channels, within 20% degradation for omnidirectional stretching (up to 70% strain at 0°, up to 90% strain at 30°, 110% strain at 60°, and more than 280% strain at 90°), and within 10% change against 100 times repetitive 50% strain stretching. Furthermore, fig. S12 demonstrates device durability against repetitive crumpling, and fig. S13 briefly and schematically depicts experimental setups for the above device characterizations.

Demonstrations of shape-conformable wrapping passive photo-monitoring of transformable objects

The aforementioned fundamental device characteristics revealed the proposed stretchable PTE sensor sheet that independently monitors objects from their shape, size, and even motions. Figure 3 demonstrates simple shape-conformable photo-monitoring with the device serving the above purpose. The device was firmly wrapped around a balloon tube, which can be controlled by a manual pump (Fig. 3, A and B). In addition, other types of CNT film PTE sensors with device structures shown in Fig. 3C were also attached to the balloons. Figure 3D continuously maps PTE responses of the proposed device (type A), and balloon expansion was passively detected by monitoring the associated local BBR intensity enhancement. The typical Gough-Joule effect governs this phenomenon where surface temperatures of the balloon were increased by rubber strains (from 23.6°C as the original state to 24.9°C as the expanded state). As the temperature of the target objects principally determines the BBR intensity from targets themselves based on Planck's radiation law, passive PTE responses of the device differ in response to balloon movements (Fig. 3E). These results demonstrate passive photo-monitoring–based simple deformation detection with a compact configuration where the device is just firmly wrapped around transformable objects. Meanwhile, Fig. 3F clarifies that attaching other device configurations (types B to D of Fig. 3C) results in disconnections with device stretching induced by the balloon expansion. Here, type B only exhibits flexibility on the channel, type C lacks stretchability on the channel, and type D has fragile electrodes, inferring the advantageous functionality of the proposed device.
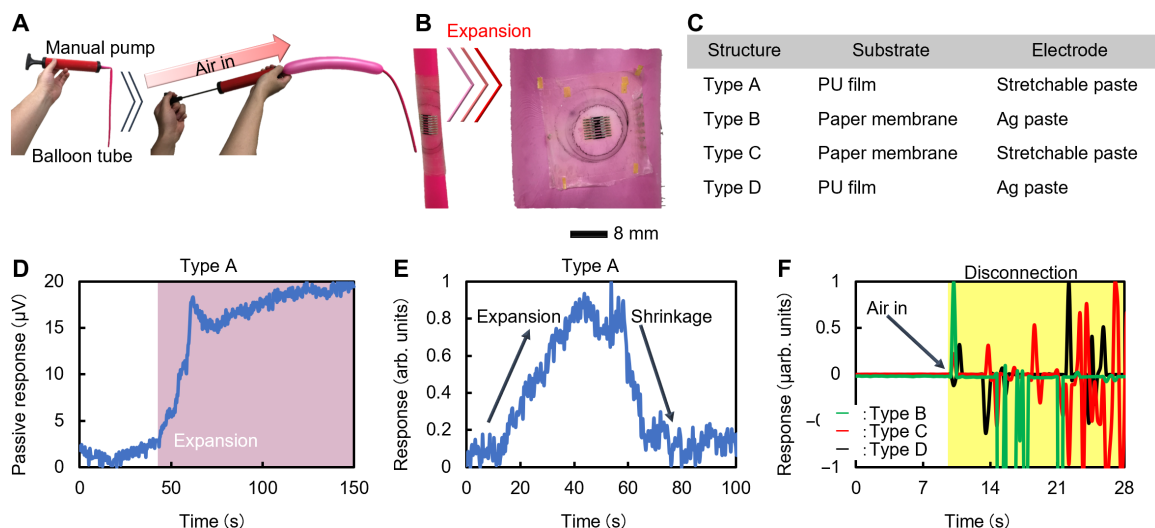

Structure	Substrate	Electrode
Type A	PU film	Stretchable paste
Type B	Paper membrane	Ag paste
Type C	Paper membrane	Stretchable paste
Type D	PU film	Ag paste

Fig. 3. Demonstrations of shape-conformable wrapping photo-monitoring of balloon movements. This work demonstrates BBR-induced, external source–free passive deformation detection of a balloon tube. (**A**) Photographs of the balloon tube and its expansion. (**B**) Photographs of the stretchable PTE sensor sheet, which firmly attaches to the target balloon via adhesive cream. BBR signals from the balloon itself were continuously observed by the proposed device as passive PTE responses. The outer surface temperature of the balloon was respectively measured at 23.6° and 24.9°C for original and expansion states, and this can be explained by the typical Gough-Joule effect. (**C**) To assess the significance of the presented device stretchability, other types of CNT film PTE sensors were also used. Here, type A exhibits stretchability on both the substrate and electrode, while a paper membrane substrate only obtains flexibility and a Ag paste electrode shows neither. (**D**) Change in BBR-induced passive PTE responses owing to the balloon expansion obtained by the proposed device (type A). (**E**) The observed passive response change was associated with the surface temperature increment during balloon expansion. (**F**) BBR-induced passive responses of the remaining three types of devices (C), wrapped around the balloon. Device breakages caused by balloon expansion were observed in each case, inferring an advantage of stretchability on both the substrate and electrode.
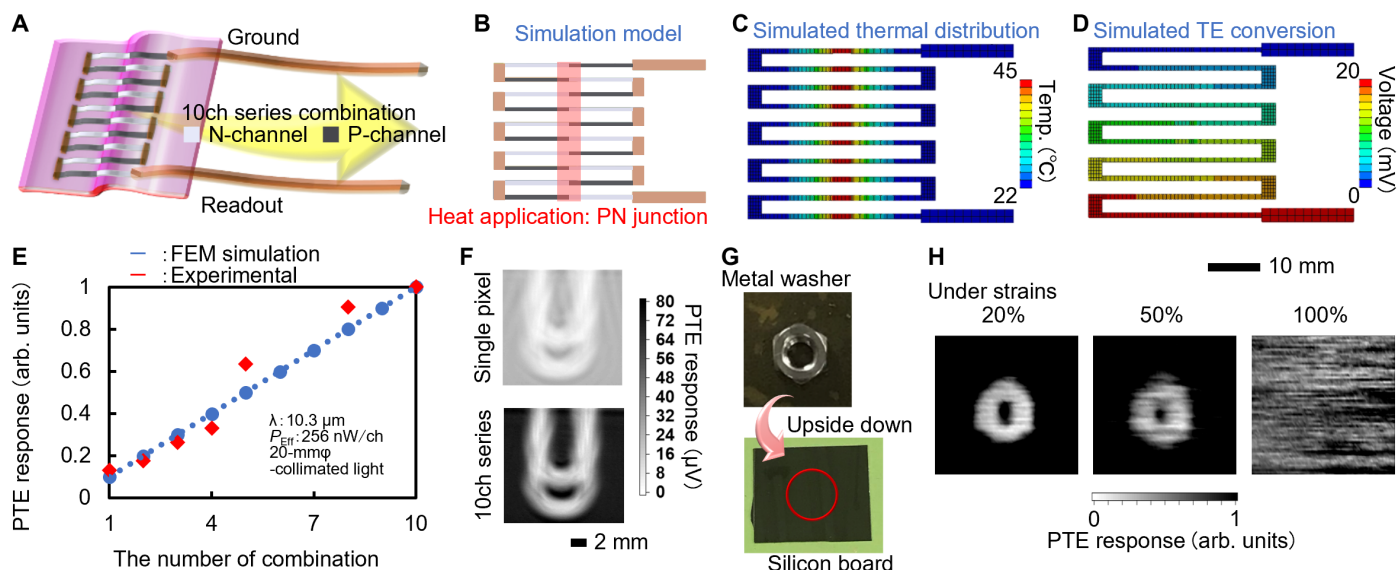
Fig. 4. Series multipixel integration of CNT film channels and its PTE imaging performances. (**A**) Schematic of the series multi-PN-pixel integration. CNT films were precisely confined and arrayed via the UV laser processing and selective suction filtration process (fig. S14), as described in the "Selective suction CNT film patterning" section in Materials and Methods. (**B** and **C**) Simulated device behaviors of the photo-induced steady-state thermal distribution and TE conversion on the proposed integrated channel (**D**). Figure S15 and the "FEM simulation of steady-state thermal distribution" and "FEM simulation of TE conversion" sections in Materials and Methods describe the corresponding detailed simulation conditions. (**E**) Changes in PTE responses of CNT film PTE sensors with different number of the series pixel integration under external FIR ($\lambda = 10.3\ \mu m$) irradiation. The final photo-detection sensitivities at the broad IR regions of the proposed device are shown in fig. S16. The device was covered with a thin metallic slit film; thus, the external collimated light irradiation was confined to the PN junction array–based photo-detection interface. (**F**) Nondestructive transmissive THz ($\lambda = 577\ \mu m$) imaging of a concealed metallic clip obtained by CNT film PTE sensors with different number of the series pixel integration. (**G**) Nondestructive transmissive THz imaging of a concealed metallic washer with different strain magnitudes on the proposed device (**H**). Figure S17 and the "Single-pixel XY imaging" section in Materials and Methods describe the corresponding detailed experimental conditions.

Multipixel integration for the photo-detection sensitivity enhancement

The photo-detection sensitivity enhancement also needs to be addressed as an important step toward promoting shape-conformable BBR-based passive photo-monitoring techniques. Specifically, extremely sensitive uncooled (NEP) values of sub–5 pWHz$^{-1/2}$ have been reported for advanced solid-state THz-IR photo-detectors (*28–30*). These overcome the technical challenge for the passive photo-monitoring caused by the weaker intensity of BBR than that of external photo-sources (*31*). In contrast, the uncooled NEP value of our existing PN junction–type CNT film PTE sensor still remains over 30 pWHz$^{-1/2}$ (*32*), underscoring an urgent need for the photo-detection sensitivity enhancement. To tackle this, a series multipixel integration of PN junction–type CNT films (fig. S14) was designed. Figure 4A schematically describes the structure of the proposed multipixel integration, and the channel region consists of 10 pixels of 100-μm-width CNT films. Respective P- and N-type regions were arranged to connect to each other alternatively and consecutively via electrode relay points, and a 10-PN junction, which was arrayed in the pixel integration direction, corresponds to the photo-detection interface (Fig. 4, B to D, and fig. S15, A and B). The series multi-PN-pixel combination, inspired by the heat conduction model of multipixel TE generator modules (*33*), was designed by UV laser processing and selective suction CNT film patterning, effectively improving photo-detection area efficiencies. Hence, up to 10-fold simulation and experimental PTE response enhancements were performed (Fig. 4E and fig. S15C). A minimum NEP value of the proposed device structure, under uncooled nonvacuum photo-detection in broad IR regions, reached sub–5 pWHz$^{-1/2}$ [3.87 pWHz$^{-1/2}$

in $\lambda = 10.3\ \mu m$ ($\Delta V = 12$ mV, $P_{Eff} = 256$ nW per channel, beam spot: 20-mmφ-collimated), 4.5 pWHz$^{-1/2}$ in $\lambda = 4.33\ \mu m$ ($\Delta V = 10.4$ mV, $P_{Eff} = 260$ nW/ch, beam spot: 5-mmφ-collimated), and 8.68 pWHz$^{-1/2}$ in $\lambda = 870$ nm ($\Delta V = 3.22$ mV, $P_{Eff} = 155$ nW/ch, beam spot: 5-mmφ-collimated), for the device with the resistance of 20 kilohms], which is comparable with those of the aforementioned solid-state photo-detectors. Here, the total channel length and width of the device presented are respectively 3 and 1 mm (100 μm width/ch × 10), and D^* values in broad IR regions are shown in fig. S16. Considering the mechanical-optical stability shown in this work earlier (within 20% degradation with omnidirectional strains; Fig. 2H), the proposed device exhibits photo-detection sensitivities for even stretched conditions (up to 11 pWHz$^{-1/2}$) comparable with those of existing rigid detectors, such as 20 pWHz$^{-1/2}$ of the Micro Electro Mechanical Systems (MEMS) bolometer (*18*).

Figure 4F and fig. S17A then demonstrate transmissive THz imaging measurements using the proposed device with different numbers of pixel integrations (single-pixel and 10-pixel integration). A metallic clip, concealed on an opaque silicon board, was nondestructively identified by detecting locally attenuated transmission signals corresponding to its shape and location. Moreover, the results indicate that the series multipixel integration exhibits a higher intensity of photo-response signal attenuation at the location of the targets, resulting in more vivid visualizations. In addition, another THz imaging demonstrations under device stretching (fig. S17B) were performed. A metallic washer, concealed on the board as shown in Fig. 4G, was visualized in line with the above cases of the clip, and the device properly captured PTE images before disconnection (Fig. 4H). Specifically, changes in PTE image quality with different

strain intensities similarly tend to the earlier mechanical device characterization (Fig. 2G). The "Single-pixel *XY* imaging" section in Materials and Methods describes the corresponding experimental details. The pixel integration and the associated larger channel size than that of the single-pixel structure generally cause spatial resolution degradation for imaging measurements, as long as the used wavelength is smaller than the channel size. However, techniques of fine processing and integration of multiple pixels would relax the above problem by managing the total channel width of the integrated structure to be adjusted within the channel width of the original single-pixel device. In this work, the minimum processing resolution of a UV laser being used for patterning fabrication of CNT filtration masks is 10 μm. Therefore, designing a 10-pixel-integrated structure consisting of a channel array with width and pitch within 25 μm each could manage the total channel width within the original single-pixel device width of 500 μm. The results here also infer further functionalization (i.e., stretchability) on existing flexible broadband photo-imagers. The uniqueness of sensitive broadband photo-detection ranging from the sub-THz (*20*) to the near-IR (NIR) regions promoted the field of stretchable photo-detectors, where characterizations of elastic narrowband-absorbent materials have mainly been performed (*34*–*36*).

BBR-based passive sensing and around-view imaging of liquids by sensor sheet wrapping

By making the most of the presented device characteristics, Fig. 5 (A to C) first demonstrates simple liquid monitoring. Figure 5A briefly and schematically presents the setup of liquid temperature monitoring measurements. The proposed stretchable PTE sensor sheet was firmly patched onto the outer surface of an opaque polyvinyl chloride (PVC) pipe. Figure 5B continuously maps PTE responses of the device, and cold (10°C) and hot (50°C) water flowing inside the PVC pipe were passively detected by monitoring the associated local BBR intensity changes. The above sensing was
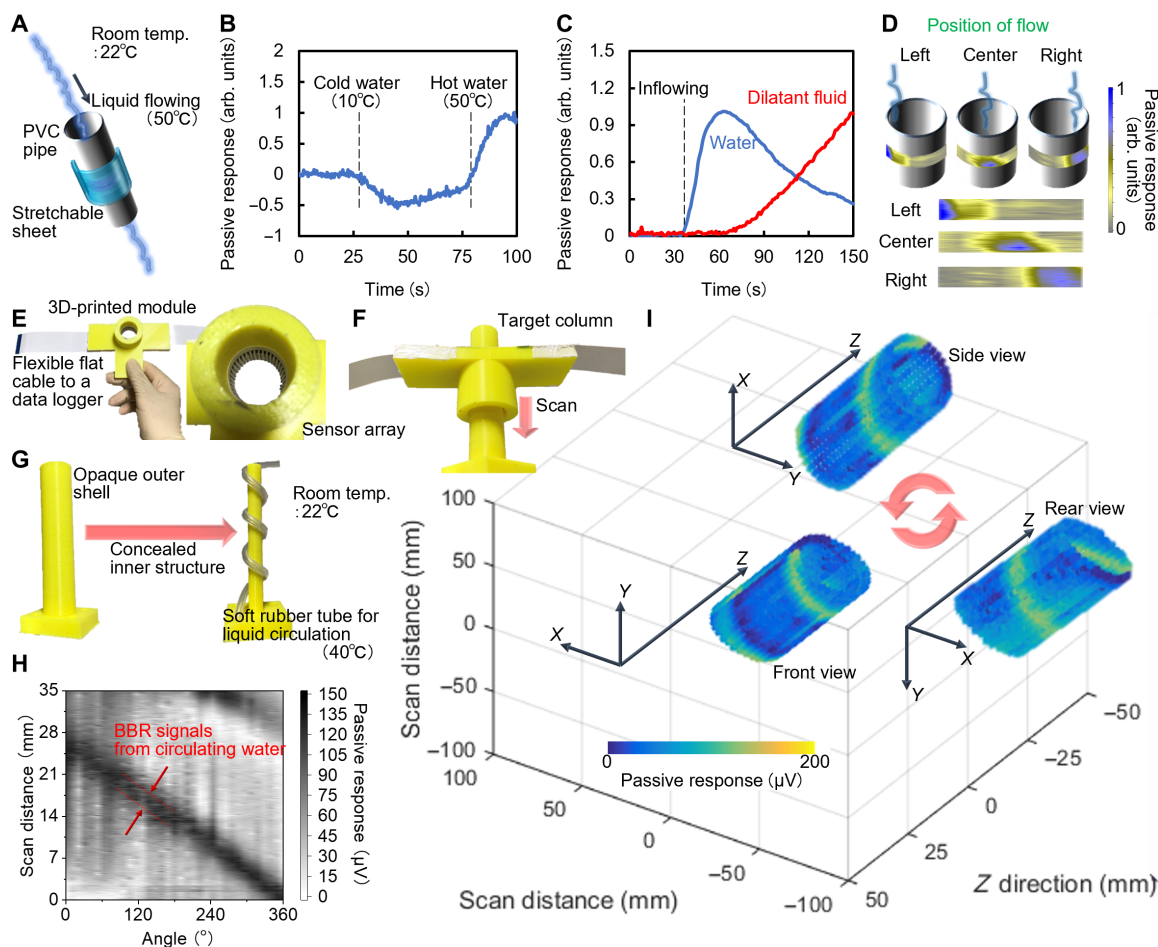

Fig. 5. BBR-based passive on-site dynamic photo-monitoring of the fundamental liquid properties by sensor sheet wrapping. (**A**) Simple experimental setup for monitoring the (**B**) temperature, (**C**) viscosity, and (**D**) position for liquids flowing inside an opaque pipe. Here, a device with a 10-pixel PTE sensor array was used (D). The device flexibility further enables compact 360° around-view imaging. This work demonstrates 3D imaging of the liquid flowing based on BBR sensing. (**E**) Photographs of a portable 360° around-view PTE imager. The "3D imaging" section in Materials and Methods describes the corresponding experimental details. Here, a 36-pixel PTE sensor array sheet based on CNT film channels is attached inside an aperture of a 3D-printed module. (**F**) Photograph of a monitoring target being scanned by the 360° imager. (**G**) Photographs of the monitoring target. The target consists of three layers: an opaque outer cylinder shell, an inner column, and a soft rubber liquid circulation tube between them, which spirally attaches to the inner column. The outer shell and the inner column were respectively prepared by a 3D printer, and the "3D imaging" section in Materials and Methods describes the corresponding experimental details. (**H**) PTE image obtained by the 360° around-view monitoring of the target column. (**I**) 3D PTE image reconstruction of the target column.

performed in a nondestructive manner where BBR passed through a wall of the opaque PVC pipe. The room temperature outside the target pipe was maintained at a constant 22°C. Changes in passive PTE responses of the device corresponding to the BBR intensity were in good agreement with that of temperatures of cold and hot water relative to the outside room temperature ($\Delta V_{Hot}/\Delta V_{Cool} = 2.2$, $T_{Hot-Out}/T_{Out-Cool} = 2.3$; ΔV, photo-response; T, temperature). The response time given an adequate experimental setup would potentially be accelerated to be a few milliseconds, corresponding to the device time constant against active photo-irradiation (fig. S18). Figure 5C further demonstrates flowing liquid viscosity monitoring. Both normal water and dilatant fluid were prepared at the same liquid temperature (50°C) and poured in the PVC pipe, respectively. The result passively detects the liquid flowing speed by mapping time-varying waveforms of the changes in BBR-induced PTE signals of the device. These assessments represent that the proposed device allows understanding the fundamental physical properties of concealed target liquids (e.g., temperature and viscosity) with passive photo-monitoring–based simple experimental configurations without using external sources.

Meanwhile, the presented device wrapping approach facilitates multi–viewing angle imaging and the associated optical information acquisition from multiple points of 3D target objects. Figure 5D and fig. S19A first visualized liquid flow positions inside the PVC pipe in a multi–viewing angle. As fig. S19B briefly depicts a sectional scheme of the experimental setup, a device with a 10-pixel PTE sensor array was firmly wrapped around the pipe. The liquid flowing at different positions can be collectively captured by comprehensively detecting the associated BBR from the liquids with each device pixel in a 120° viewing angle. Figure S19C introduces a possible use with the device wrapping. The "Multipixel PTE signal readout" section in Materials and Methods describes the corresponding experimental details. Furthermore, Fig. 5 (E to I) demonstrates compact 360° around-view imaging of 3D objects without using bulky rotation stages. Here, a portable 360° around-view PTE imager consisting of a 36-pixel CNT film channel array was fabricated (Fig. 5E), and a supporting module of the imager was prepared by using a 3D printer. An opaque column, inside which a spirally wrapped soft rubber liquid circulation tube was concealed, was the target, and its entire outer surface was covered with the imager as shown in Fig. 5 (F and G). The target was inserted into the module, and then a linear scan movement of the device resulted in obtaining a 360° around-view PTE image. The obtained image comprehensively visualizes the liquid circulation (40°C), which was confined inside the tube, based on locally enhanced BBR-induced passive PTE responses of each device pixel corresponding to the location of the liquid. Figure 5I finally reconstructs a 3D image of the concealed target liquid circulation by combining the 360° PTE image and spatial coordinate of each pixel in a nondestructive and external source–free manner. Figure S20 demonstrates that BBR-induced PTE conversion originating from the liquid dominantly accounts for the total device response compared to that from the external experimental environment. The "3D imaging" section in Materials and Methods describes the corresponding experimental details.

On-site dynamic passive in-liquid chemical photo-monitoring by sensor sheet wrapping

By incorporating previous efforts in this work, Fig. 6 (A to I) finally demonstrates simple nonsampling, source-free, and label-free on-site

dynamic passive photo-monitoring of in-liquid chemicals. Figure 6 (A and B) briefly depicts the concept and setup of the measurements. The proposed stretchable PTE sensor sheet was wrapped around a soft rubber tube of a thermostatic liquid circulation system (fig. S21), and chemical substances were dissolved in a 40°C purified water solvent. The room temperature outside the tube was maintained at a constant 22°C. Figure S22 presents passive photo-response change behaviors of the device during chemical dissolution. The obtained results indicate that the chemical dissolution triggers reductions in BBR-induced passive PTE response of the device. The obtained result also presents the above phenomenon that properly occurred by using both experimental setups with a rigid device configuration (optical path length: 1 mm to the tube) and the direct device wrapping configuration. Results in Fig. 6C and fig. S23 further depict that the higher concentrations of in-liquid chemicals induced larger magnitudes of the device photo-response reduction. In other words, the solution concentration potentially governs the BBR intensity from the solvents and associated passive PTE responses of the device. Here, fig. S24A demonstrates a spectral analysis and clarified higher photo-absorption in broad IR regions with in-liquid chemicals under higher solution concentration. This spectral measurement was performed by using the attenuated total reflection (ATR) function [Fourier transform IR (FTIR) spectroscopy], and the purified water (solvent of target chemicals) was measured as the reference to extract photo-absorption with in-liquid chemicals themselves. Owing to the constant liquid temperature, in-liquid chemicals locally absorb BBR from the solvent, resulting in reductions of the BBR intensity to be detected by the device and differing reduction magnitudes depending on solution concentrations. Figure S24B then compares the device photo-response behavior and spectral estimation under changing concentrations of in-liquid chemicals. The change in reduction values of BBR-induced passive PTE responses of the device and integral values of the spectral photo-absorptance with in-liquid chemicals exhibit good agreement for different solution concentrations. Here, integral values of the spectral photo-absorbance were used as a comparison index for validating device performances owing to the broadband operation of the CNT film PTE sensor. To sum up these, the proposed device wrapping strategy enables on-site dynamic solution concentration monitoring as shown in Fig. 6D. The detectable concentration in this work finally ranges from 50 to 20,000 mg/dl, e.g., glucose solution, and these potentially satisfy sensitivity requirements for diverse applications including diabetes diagnoses (*37*) and plant or fruit sugar content measurements (*38*). Simultaneously, Fig. 6E demonstrates 360° around-view visualization of changes in the solution concentration. This was inspired by the efforts in Fig. 5 (E to I) and achieved by continuously monitoring the local absorption change of BBR from the solvent with in-liquid chemicals for different concentrations in a 360° around-view point. These imaging applications potentially ease the understanding of chemical reactions at multiple points in a large area of 3D environments.

Meanwhile, Fig. 6 (F to I) validates the accuracy of the presented technology from another viewpoint of solution types (glucose solution and tannic solution). The operating conditions, such as the room temperature (constant 22°C), liquid temperature (constant 40°C), and solution concentration (333 mg/dl), were set to be the same for both targets. For the spectral analysis, each parameter involved in experimental measurements was examined by the ATR-FTIR as follows: the theoretical value of the BBR intensity at a
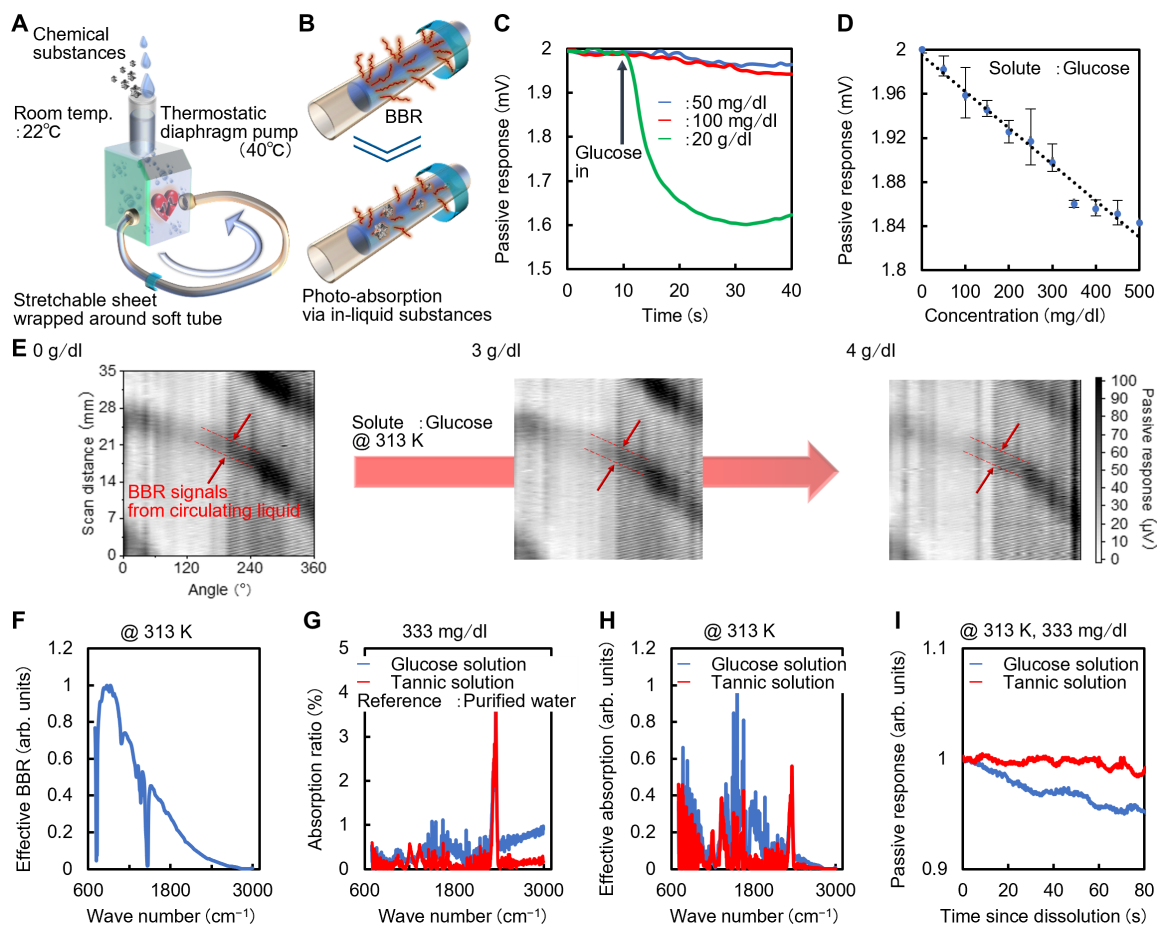
Fig. 6. BBR-based, nonsampling, and label-free passive on-site dynamic photo-monitoring of in-liquid chemical concentrations. (**A** and **B**) Schematics of the concept and measurement setups. (**C**) Changes in BBR-induced passive responses of the proposed device with different amounts of glucose powder dissolution. (**D**) Changes in BBR-induced passive PTE responses of the device versus glucose solution concentrations with a range of 50 to 500 mg/dl. Glucose powder was dissolved in 1 dl of the purified water solvent, 50 mg each, for a total of 10 times. (**E**) Comparison in PTE images of concealed 3D liquid flowing obtained by the portable 360° around-view imager (Fig. 5, E to I) for different amounts of chemical dissolution. (**F**) Spectral graph of the effective BBR intensity from the circulating solvent water at a constant temperature of 40°C. (**G**) Spectral graph comparing photo-absorptance values of in-liquid glucose and tannic at the same concentration. (**H**) Spectral graph comparing magnitudes of BBR absorption on in-liquid glucose and tannic at the same concentration. (**I**) Changes in BBR-induced passive PTE responses of the proposed device with glucose and tannic dissolution at the same concentration.

temperature of 40°C (I_{BBR}, derived from Planck's radiation law; fig. S25A), transmittance of a low-pass filter (t_{Low}, black polyethylene; fig. S25B), the soft liquid circulation tube (t_{Tube}; fig. S25C), the PU sealing layer (t_{Seal}, derived from fig. S2), and photo-absorptance of the CNT film channel (A_{CNT}; fig. S25D). The practical BBR and photo-detection spectrum can be respectively expressed by $I_{BBR} \times t_{Low}$ ($I_{Eff\text{-}BBR}$; Fig. 6F) and $I_{Eff\text{-}BBR} \times t_{Tube} \times t_{Seal} \times A_{CNT}$ (ΔV_{Eff}; fig. S25E). Furthermore, together with photo-absorptance of 333 mg/dl concentration in-liquid glucose and tannic (A_{Glu} and A_{Tan}; Fig. 6G), spectral estimation of the BBR absorption from the solvent with both in-liquid chemicals can be obtained ($\Delta v_{Eff\text{-}Glu}$: $\Delta V_{Eff} \times A_{Glu}$ and $\Delta v_{Eff\text{-}Tan}$: $\Delta V_{Eff} \times A_{Tan}$; Fig. 6H). The ratio of $\Delta v_{Eff\text{-}Glu}$ to $\Delta v_{Eff\text{-}Tan}$ was calculated to be 2.4, inferring that the glucose dissolution causes a higher reduction in BBR-induced passive PTE responses than that by the tannic dissolution. Simultaneously, experimental monitoring on both solutions was performed (Fig. 6I), and the reduction magnitude ratio of device photo-responses for the glucose solution to that for the tannic solution was calculated to be 2.9. The experimental

tendency was certainly aligned with the spectral estimation, and these assessments help understand specific behaviors of in-liquid chemicals for the BBR-based passive photo-monitoring scheme depending on types of chemicals. The above assessments represent the spectral simulation for the BBR-based passive in-liquid chemical monitoring to validate the performances of the actual device measurements. Each necessary spectrum was obtained by FTIR measurements in advance to the actual device monitoring, including the reference absorption of the CNT film channel and the target in-liquid chemicals. To complete even such spectral evaluations by the device itself, and further bring selectivity for the target in-liquid chemicals, the future integration of the deformable PTE sensor and stretchable broadband tunable filter would greatly contribute to this issue. Figure S26 briefly describes the above condition.

To sum up these, fig. S27 represents the simple conceptual diagram of the passive in-liquid measurements. The presented technology effectively uses the broad IR radiation naturally originating from liquid solvents, local photo-absorption by in-liquid chemical

substances to be monitored, and broad IR detection of the proposed scanner sheet device. This external source–free photo-monitoring configuration can be categorized as passive sensing techniques. Achievements in this work are inspired by previous methods of gas detection in the atmosphere using the broad IR radiation from the ground surface (39–42). In this gas detection method, IR detector devices continuously capture BBR from the ground, and gas leakages and the associated local IR absorption with gas molecules can be identified on the basis of signal changes in detector responses. While remote gas monitoring satellites are often equipped with multiple narrowband photo-detectors to cover wide ranges of short-wavelength IR regions, even the use of general photo-thermal detectors such as uncooled broadband bolometers functions well for fundamental BBR-based passive gas sensing applications in long-wavelength IR regions (43). Including the above, conventional passive sensing studies have been mainly focused on gas and solid targets; however, this work handles liquid configurations.

DISCUSSION

While device design on the stretchable PTE sensor sheet has promoted the BBR-based passive photo-monitoring techniques as was intended, further efforts on the following topics potentially accelerate developing the scheme presented here. Wireless device driving is one of them (fig. S28), for example. Figure S29 demonstrates the wireless PTE signal readout of CNT film photo-detectors, providing a potential solution for realizing mobile applications, being independent of the operating environment. In particular, implementing high-operability wireless circuits on stretchable photo-sensor sheets would provide a useful combination for various practical situations, such as portable all-in-one industrial liquid quality testing and long-term noninvasive botanical liquid nutrient monitoring on stems or roots. In addition, applications of a roll-to-roll device printing (44, 45) are considered to be another key step to further functionalize the proposed scheme. Specifically, the subsequent large-scale and high-density pixel integration enhances the data acquisition efficiency of target physical information and realizes real-time massive monitoring. Furthermore, multipoint sensing with each pixel channel is expected to lead to functional multimodal device driving. Recent progress on multimodal sensing devices (46–48) provides increased focus on them, and the proposed device potentially enables measuring the multifactor liquid quality, target temperature, and physical motion, which are yet to be collectively captured.

In conclusion, this study introduced the nondestructive and nonsampling, photo-source–free, and label-free passive on-site dynamic in-liquid chemical monitoring approach by simply wrapping the mechanically stretchable and freely deformable PTE uncooled broadband THz-IR sensor patch sheets around soft flow channels. This system combines stretchable electronics, CNT-based materials, PTE conversion, BBR-based passive photo-sensing, and spectroscopic analysis. The proposed patch sheet collectively satisfies sensitive broadband THz-IR photo-detection and optical stability against mechanical deformations, being advantageously ranked among existing devices (table S1). In addition to relaxing past technical difficulties on the liquid quality photo-monitoring, the obtained findings also enrich conventional BBR-based passive sensing schemes. While previous passive sensing has focused on solid object screening or gas leakage detection (49–54) using single-viewpoint rigid cameras,

this study enables fluidity-inspired free-form in-liquid chemical analysis and omnidirectional shape-conformable sensing and imaging. These strategies contribute to developing versatile environmental testing platforms where the sensor sheets are only being wrapped around arbitrary fluid channels for continuously monitoring in-liquid chemical parameters.

The presented technology currently handles solutions consisting of a single component in terms of the concentration. This method potentially facilitates user-friendly and easy-to-operate quality monitoring and impurity detection at manufacturing sites of beverages (e.g., sugar water) or industrial chemicals (e.g., chlorine bleach), medical practice fields (e.g., saline infusion), etc. Meanwhile, selectivity is an essential feature for ubiquitous liquid chemical testing purposes including the immediate and sustainable analysis of constituents in domestic and industrial wastewater. To achieve selectivity with the proposed system, an integration of mechanically stretchable and optically tunable broadband filters with the CNT film PTE sensor needs to be tackled, as mentioned earlier. This strategy would facilitate selective concentration inspections based on the peak absorption wavelength information for each chemical while maintaining the compactness and simplicity of the entire system configuration. Existing broadband tunable filters mainly exhibit rigid housing structures, and investigations for demonstrating promising stretchable tunable broadband filters are yet to be well completed. In other words, a study on stretchable tunable broadband filters is a noteworthy topic in broad research fields including photonics and flexible and stretchable electronics. Therefore, demonstrating the above concept and realizing the associated on-site dynamic selectivity of nonsampling and label-free passive in-liquid chemical concentration evaluations are indispensable steps for the next scope. Relatedly, the effective use of lock-in amplifiers is thought to enhance the versatility of the proposed technology. This work used the thermostatic temperature control system for liquid targets to avoid the interference from the room temperature outside the flowing channels. The use of lock-in amplifiers then would suppress the room temperature interference via periodic oscillations between the device and liquid tube, even under the condition that the temperatures of the target liquid and outside air are uniform.

In addition to the on-site detection of chemical dissolution demonstrated in this work, the presented wrapping passive photo-sensing approach would monitor chemical reactions between in-liquid chemicals. The broad and high-efficiency THz absorption characteristic of the used semiconducting and metallic mixed-type SWCNT film (55) further allows the device usage for fundamental THz monitoring applications. In the same way that external THz irradiation enables nondestructive remote gas reaction sensing (fig. S30), potential example includes hydrolysis of sucrose in acid solvents where measurements of reaction heat–induced BBR signals facilitate on-site in-liquid chemical reaction monitoring.

MATERIALS AND METHODS
Selective suction CNT film patterning
Suction CNT film filtration was performed for the selective channel patterning. A semiconducting and metallic mixed-type SWCNT solution (Zeon Co.) was dripped on a membrane filter (70 μm thick, 200-nm pore; C020A025A, Advantec Ltd.), which was covered with a polyimide (PI) mask (5 μm thick; Kapton, Du Pont-Toray Co.), and then vacuumed (vacuum pump: MVP015, Pfeiffer Vacuum

Technology AG). PI mask was processed with a UV laser ($\lambda = 355$ nm; LWL-3030-T06, Sigma Koki Co.), and the minimum processing resolution is 10 µm. The typical channel length, channel width, channel thickness, and channel pitch are 4 mm, 500 µm, 1 µm, and 500 µm for the single-pixel and multipixel device and 3 mm, 100 µm, 1 µm, and 200 µm for the multipixel-series-integrated device, respectively.

Chemical carrier doping
Liquid coating chemical doping was used as the carrier injection method for CNT film channels. By dripping a mixed dopant of KOH aqueous solution (0.5 M; Tokyo Chemical Industry Co. Ltd.) and 15-crown 5-ether aqueous solution (0.5 M; Tokyo Chemical Industry Co. Ltd.) onto an originally P-type CNT film, the anion (K^+) is trapped by the crown ether with respect to the freely acting cation (OH^-) and locally changes to an N-type at the point of application. The doping was performed under atmospheric pressure and room temperature, and the device can be driven as a photo-sensor immediately after drying. Figure S1 (B to D) further depicts the corresponding experimental conditions.

Stretchable PTE sensor sheet design
To fabricate stretchable PTE sensor sheets, selectively suction-filtered CNT film channels were first transferred onto a thin PU substrate (8 µm thick; Silklon, NES85SW, Okura Industrial Co.) via a double-sided adhesive PI tape (80 µm thick; Scotch92, 3M Japan Ltd.). The stiffened area, located beneath the channel, was then formed across the thin PU substrate. Epoxy resin (ET, Devcon Ltd.) was printed on different types of PU substrate (70 µm thick; Ecellent, SHM101-PUR, Sheedom Co.) with a mask, with an aperture of 7 mm × 3.5 mm × 0.1 mm volume and cured for 1 hour at 60°C. For the elastic electrode, composite paste (SX-ECA, Cemedine Co.) was used. The conducting paste was printed on the thin PU substrate with a 0.1-mm-thick mask and annealed for 30 min at 100°C. The annealed stretchable electrode gave a volume electric resistivity of 1.1×10^{-4} ohm·cm. After the chemical carrier doping onto the CNT film channels, the described device structure was covered with another thin PU film and sealed at 100°C. Last, the device conduction can be obtained by applying the stretchable conducting paste through holes and the device annealing. For evaluating the adhesion strength of the epoxy stiffener, cellulose tape (Nichiban Co.) was used.

Stretchable substrate and electrode
A tensile tester (EZ Test, Shimadzu Co.) was used to evaluate the electrical resistance stability of PU substrate–elastic electrode composites against repetitive stretching. The stretching speed of target substrates and electrodes was set at 60 mm/min. The resistance value signals were continuously recorded on a digital multimeter 34461A, Keysight Technologies Inc.

PTE response against mechanical deformations
Here, the photo-response stability of the proposed PTE sensor sheet against mechanical deformations was investigated, including stretching and vacuum crumpling. For device stretching, the device was connected to a multiplexer data logger (34980A-34923A/T, Keysight Technologies Inc.) and digital stepping motors (Motorized Stage, Sigma Koki Co.). Operating conditions of the data logger were set as follows: scan resolution of 100 nV and scan speed of 10 Hz. The minimum stepping resolution of the digital stage is 500 nm, and a

scan step was set at 100 µm here. Figure S13A schematically depicts the measurement setup of the device stretching. PTE response signals induced by external photo-irradiation were continuously recorded on the multiplexer data logger, while both ends of the device were fixed to two stepping motor stages along the stretching direction. Stretching scan speed was set at 1 mm/s. In addition, PTE measurements were performed by synchronously controlling the multiplexer data logger and digital stepping motor using LabVIEW programs and General Purpose Interface Bus (GPIB) cables.

Figure S13D shows the measurement setup for device crumpling. The proposed device was fixed to an aperture chamber, and PTE response signals induced by external photo-irradiation were continuously recorded on the digital data logger, while the device was consistently crumpled by using the aforementioned vacuum pump.

FEM simulation of strain distribution
To understand the elastic behavior of the stiffened area of the PU substrate, a 3D linear FEM analysis was performed with Siemens NX 10.0.3.5. As the design is symmetric, only a quarter of the design has to be modeled. The top view is shown in fig. S6A. Symmetry constraints were applied on the left and bottom polygon edge. Furthermore, a displacement of 3.5 mm was applied on the right polygon edge to apply a strain of 50% to the whole structure (74% of the unsupported part, i.e., substrate without stiffener). Tetra 10 elements, pyramid-shaped elements with 10 nodes, were used with mesh size of 26.8 and 45.9 µm to model the stiffener and substrate, respectively. This resulted in a model with 530,501 elements and 868,156 nodes. Young's modulus and Poisson ratio of the epoxy stiffener were set to 3 GPa and 0.33, respectively (56–58). Young's modulus and Poisson ratio of the PU substrate were set to 6.3 MPa and 0.48, respectively (59, 60). Although large deformations were applied in the simulations, a linear FEM analysis was conducted to reduce the calculation time from days to minutes; this was necessary because of the large number of elements. Stiffener topologies are depicted in fig. S6B. Figure 1C shows the strain field of the analysis. The red squares in the figure represent the modeled part. The figure indicates that the strain in the top surface just above the stiffener is virtually 0. The surface strain then increases from the center to the edge in the stiffener while increasing significantly outside of the stiffener.

FEM simulation of steady-state thermal distribution
ANSYS software was used for the steady-state thermal analysis to investigate the heat distribution and temperature gradient in the channel during photo-absorption and to clarify the associated behaviors of the proposed multipixel-series-integrated PTE sensor sheet. Heat flows were applied to analysis models based on the assumption that CNT films are efficient at photo-absorption. By setting the thermophysical property value of the CNT film channel and the electrode, the following heat conduction equation was solved using FEM

$$\rho C \frac{\partial T}{\partial t} = k \left(\frac{\partial^2}{\partial x^2} + \frac{\partial^2}{\partial y^2} + \frac{\partial^2}{\partial z^2} \right) T + Q \tag{1}$$

Here, ρ, C, k, T, and Q are the density, heat capacity, thermal conductivity, absolute temperature, and total heat flow, respectively (55). The thermophysical property values of the CNT film are as follows: k, 10 W/mK (23); emissivity ε, 0.9 (calculated from Kirchhoff's law of thermal radiation: ε = absorptivity α). The outside temperature was set to a constant 295 K.

FEM simulation of TE conversion

TE analysis (ANSYS software) was used to further investigate behaviors of the proposed multipixel-series-integrated PTE sensor sheet. Calculation of the photo-induced voltage signals is based on the typical Seebeck effect, and fig. S15A presents a simplified TE conversion analysis model. In addition to the thermophysical conditions mentioned earlier, Seebeck coefficient and electrical conductivity of CNT films were respectively set as follows (23): $38\,\mu V/K$ and $1.51 \times 10^3\,Scm^{-1}$ for undoped CNT films and $-33\,\mu V/K$ and $2.05 \times 10^3\,Scm^{-1}$ for doped CNT films.

Multipixel PTE signal readout

Photo-induced direct current-voltage response signals of the multipixel CNT film PTE sensor array sheet were recorded on the aforementioned multiplexer data logger. Up to eight terminal blocks can be mounted on one multiplexer data logger, and there can be up to 80 elements per terminal block. The scan resolution for the multipixel readout is 100 nV, the same as the condition for the single-pixel readout. The multipixel readout speed, which exhibits trade-off with the scan resolution, was set at 50 channels/s. Regardless of the number of pixels, photo-sensor sheets were directly connected with the multiplexer data logger without passing through an amplifier.

Single-pixel *XY* imaging

To obtain the transmissive 2D images using a single-pixel CNT film PTE sensor sheet (Fig. 4, F and H), the device was connected to a digital data logger. Imaging objects were attached to a two-axis moving stage consisting of a combination of two of the aforementioned one-axis stepping motors. The photo-response at each point was recorded on the digital data logger while controlling the *XY* position of imaging objects at every 100 μm. The stepping scan speed was set at 1 mm/s.

3D imaging

The aperture module, the outer shell of the target, and the inner column in Fig. 5 (E to I) were respectively prepared by using a 3D printer (Value3D Magix MF-2500EP II, Mutoh Industries Ltd.). Each model was designed on 3D CAD software (Autodesk Tinkercad). The minimum processing accuracy was 50 μm in the *XY* axis and 100 μm in the *Z* axis. Polylactic acid was used for the printing resins. The size of each component was as follows: aperture, 25 mmφ and 40 mm in height; outer shell, 22 mmφ (outer), 20 mmφ (inner), and 100 mm in height; and inner column, 10 mmφ and 100 mm in height. Here, a 36-pixel CNT film PTE sensor array sheet was attached to the inner surface of the aperture. The inside and outside diameters of a soft rubber liquid circulation tube are 3 and 5 mm, respectively.

The portable 360° around-view PTE imager was connected to a *Z*-axis stepping motor and the aforementioned multiplexer data logger. After inserting the target column to the imager, module scanning was performed at every 100 μm for a total distance of 35 mm. The 3D structure in the *XYZ* space (*XY*, plane coordinates of each pixel; *Z*, scan distance) was reconstructed on the basis of the CAD design. Then, a 4D diagram was coordinated by referring to the obtained BBR-based passive PTE response signals at each pixel.

Thermal durability and optical stability evaluation of CNT film PTE sensors

A digital programmable hotplate (1-7565-01 Digital Hot Plate To 430°C, HP-1SA, AS ONE Co.) was used. Photo-response signals of

the proposed CNT film PTE sensor sheet were continuously recorded on the multiplexer data logger during device annealing. A NIR LED was mounted on the digital stepping motor and suspended above the channel. To avoid heat damage, the LED was kept away from the hotplate except for the timing of photo-response measurements.

Photo-sources

Four types of photo-sources were used, namely, a frequency multiplier in the THz band (λ = 577 μm, 4-mmφ-collimated irradiation, 520- to 532-GHz Custom Modular Tx-Transmitter, Virginia Diodes Inc.), a gas laser in the far-IR (FIR) band (λ = 10.3 μm, 20-mmφ-collimated irradiation/1-mmφ-fiber irradiation, CO2 Laser L4, Access Laser Co.), a quantum cascade laser in the Mid-Infrared MIR) band (λ = 4.34 μm, 5-mmφ-collimated irradiation, DFB-CW QCLs with built-in lens L12004-2310H-E, Hamamatsu Photonics K.K.), and a LED in the NIR band (λ = 870 nm, 5-mmφ-collimated irradiation, L12170, Hamamatsu Photonics K.K.). A conical horn antenna was attached to the frequency multiplier, and collimation lenses were built into other photo-sources.

Noise equivalent power evaluation

NEP determines the photo-detection sensitivity of CNT film PTE sensors based on the following equation (55)

$$\mathrm{NEP} \; = \; \frac{V_\mathrm{Noise}}{V_\mathrm{Sensitivity}} \; = \; \frac{\sqrt{4\,k_\mathrm{B}\,\mathrm{TR}}}{S_\mathrm{Eff} \times \Delta T} \times P_\mathrm{Eff} \qquad (2)$$

Here, V_Noise, $V_\mathrm{Sensitivity}$, k_B, T, R, S_Eff, ΔT, and P_Eff are the noise voltage spectral density, normalized photo-induced PTE voltage response, Boltzmann constant, absolute temperature, electrical resistance, effective Seebeck coefficient ($S_\mathrm{P\text{-}CNT\,film} - S_\mathrm{N\text{-}CNT\,film}$), photo-induced thermal gradient in the channel, and effective power of the light irradiation on the photo-detection interface, respectively.

Liquid temperature, viscosity, and flow position monitoring

For the liquid temperature, viscosity, and flow position monitoring measurements, a 10-mmφ and 2-mm-thick PVC pipe was prepared. A 100-μm-thick silicon rubber layer was attached to the proposed CNT film PTE sensor sheet, and the space above the CNT film was hollow so that direct contact between the channel region and the outer surface of the pipe could be avoided. The pipe was partially covered with the device, and target liquids were poured inside the pipe using a pipette. To prepare a dilatant liquid, a digital programmable heating magnet stirrer [1-2945-01 Hot Stirrer (Digital), HSH-1D, AS ONE Co.] was used. The temperature of the 500-ml solvent water was set to a constant 50°C, and 50 g of potato starch was dissolved at a stirring speed of 1000 rpm. The liquid volume for each measurement shown in Fig. 5 (B to D) was 10 ml.

Solution concentration monitoring

To perform the solution concentration monitoring measurements, a digital flow rate controllable diaphragm pump (Corrosion Resistant Diaphragm Quantitative Pump 20 ml/min, 1-5312-22, FEM1.02TT.18S, KNF Co.) was used. The target liquid was continuously and thermostatically heated and stirred with a water bath stirrer (Isothermal Stirrer Bath KS-1N, 1-3903-11, AS ONE Co.) under a heating temperature of 40°C and a stirring speed of 1200 rpm. Soft tubes of the

digital pump were fixed in the solution container, and the liquid circulation was constantly controlled. The flow rate and pumping frequency were set at 20 ml/min and 3 Hz. The tube was covered with the proposed stretchable PTE sensor sheet under the same condition as that mentioned in the previous section.

THz time-domain spectroscopy
THz time-domain spectroscopy (TAS7x00TS, Advantest Co.) was used to measure the absorbance spectrum and evaluate the transparency of the PU sealing mask in the THz frequency region. The THz pulse with a frequency bandwidth of 0.5 to 7 THz was emitted from a Cherenkov-type THz wave generator using a nonlinear optical crystal ($LiNbO_3$) waveguide and used to irradiate a target sample. The transmitted pulse was guided and focused onto the photoconductive antenna (PC detector) mounted on a hyper-hemispherical silicon lens. The transmission/absorption spectrum was measured under a time resolution of 2 fs, a frequency resolution of 3.8 GHz, and a scan range of 262 ps.

FTIR spectroscopy
FTIR (IRAffinity-1S, Shimadzu Co.) was used to measure the transmission/absorbance spectrum for the BBR-based passive photomonitoring of solution concentrations and to evaluate the transparency of the PU sealing mask in the IR frequency region. The spectrum measurements were performed by the ATR method. Target samples for the ATR measurements were prepared under the same conditions as those for the BBR-based passive photo-monitoring experiments. The wave number bandwidth of the ATR-FTIR ranges from 7800 to 350 cm^{-1}, and wave number resolution is 0.5 cm^{-1}. In the obtained spectrum, peak values, such as 2400 cm^{-1} in Fig. 6G, can be observed repeatedly regardless of the target samples. It is considered that this is an equipment-derived spike noise and that it does not originate from the target samples.

SUPPLEMENTARY MATERIALS
Supplementary material for this article is available at https://science.org/doi/10.1126/sciadv.abm4349

REFERENCES AND NOTES
1. T. K. Liu, H. Y. Sheu, C. N. Tseng, Environmental impact assessment of seawater desalination plant under the framework of integrated coastal management. *Desalination* **326**, 10–18 (2013).
2. S. Rehfeldt, J. Stichlmair, Measurement and prediction of multicomponent diffusion coefficients in four ternary liquid systems. *Fluid Phase Equilib.* **290**, 1–14 (2010).
3. C. E. Restrepo, J. S. Simonoff, R. Zimmerman, Causes, cost consequences, and risk implications of accidents in US hazardous liquid pipeline infrastructure. *Int. J. Crit. Infr. Prot.* **2**, 38–50 (2009).
4. M. C. Bruzzoniti, R. M. D. Carlo, C. Sarzanini, R. Maina, V. Tumiatti, Determination of copper in liquid and solid insulation for large electrical equipment by ICP-OES. Application to copper contamination assessment in power transformers. *Talanta* **99**, 703–711 (2012).
5. K. Raunkjær, T. W. Jacobsen, P. H. Nielsen, Measurement of pools of protein, carbohydrate and lipid in domestic wastewater. *Water Res.* **28**, 251–262 (1994).
6. A. Stachniuk, E. Formal, Liquid chromatography-mass spectrometry in the analysis of pesticide residues in food. *Food Anal. Methods* **9**, 1654–1665 (2016).
7. A. C. O. Costa, L. d. S. Perfeito, M. F. M. Tavares, G. A. Micke, Determination of sorbate and benzoate in beverage samples by capillary electrophoresis—Optimization of the method with inspection of ionic mobilities. *J. Chromatogr. A* **1204**, 123–127 (2008).
8. K. A. Barnes, M. L. Anderson, J. R. Stofan, K. J. Dalrymple, A. J. Reimel, T. J. Roberts, R. K. Randell, C. T. Ungaro, L. B. Baker, Normative data for sweating rate, sweat sodium concentration, and sweat sodium loss in athletes: An update and analysis by sport. *J. Sports Sci.* **37**, 2356–2366 (2019).
9. G. Cozzi, L. Ravarotto, F. Gottardo, A. L. Stefani, B. Contiero, L. Moro, M. Brscic, P. Dalvit, Short communication: Reference values for blood parameters in Holstein

dairy cows: Effects of parity, stage of lactation, and season of production. *J. Dairy Sci.* **94**, 3895–3901 (2011).
10. H. R. El-Ramady, T. A. Alshaal, S. A. Shehata, É. D.-Szabolcsy, N. Elhawat, J. Prokisch, M. Fári, L. Marton, Plant nutrition: From liquid medium to micro-farm. *Sustain. Agr. Rev.* **14**, 449–508 (2014).
11. W. Al-Faqheri, T. H. G. Thio, M. A. Qasaimeh, A. Dietzel, M. Madou, A. Al-Halhouli, Particle/cell separation on microfluidic platforms based on centrifugation effect: A review. *Microfluid. Nanofluidics* **21**, 102 (2017).
12. C. V. Nguyen, A. V. Nguyen, A. Doi, E. Dinh, T. V. Nguyen, M. Ejtemaei, D. Osborne, Advanced solid-liquid separation for dewatering fine coal tailings by combining chemical reagents and solid bowl centrifugation. *Sep. Purif. Technol.* **259**, 118172 (2021).
13. X. M. Piao, E. J. Cha, S. J. Yun, W. J. Kim, Role of exosomal miRNA in bladder cancer: A promising liquid biopsy biomarker. *Int. J. Mol. Sci.* **22**, 1713 (2021).
14. T. Kaya, G. Liu, J. Ho, K. Yelamarthi, K. Miller, J. Edwards, A. Stannard, Wearable sweat sensors: Background and current trends. *Electroanalysis* **31**, 411–421 (2019).
15. P. Gallo, S. Fabbrocino, G. Dowling, M. Salini, M. Fiori, G. Perretta, L. Serpe, Confirmatory analysis of non-steroidal anti-inflammatory drugs in bovine milk by high-performance liquid chromatography with fluorescence detection. *J. Chromatogr. A* **1217**, 2832–2839 (2010).
16. X. Wen, Q. Yang, Z. Yan, Q. Deng, Determination of cadmium and copper in water and food samples by dispersive liquid–liquid microextraction combined with UV–vis spectrophotometry. *Microchem. J.* **97**, 249–254 (2011).
17. A. Rogalski, Semiconductor detectors and focal plane arrays for far-infrared imaging. *Opto-Electron. Rev.* **21**, 406–426 (2013).
18. Y. Zhang, Y. Watanabe, S. Hosono, N. Nagai, K. Hirakawa, Room temperature, very sensitive thermometer using a doubly clamped microelectromechanical beam resonator for bolometer applications. *Appl. Phys. Lett.* **108**, 163503 (2016).
19. M. Long, Y. Wang, P. Wang, X. Zhou, H. Xia, C. Luo, S. Huang, G. Zhang, H. Yan, Z. Fan, X. Wu, X. Chen, W. Lu, W. Hu, Palladium diselenide long-wavelength infrared photodetector with high sensitivity and stability. *ACS Nano* **13**, 2511–2519 (2019).
20. K. Li, R. Yuasa, R. Utaki, M. Sun, Y. Tokumoto, D. Suzuki, Y. Kawano, Robot-assisted, source-camera-coupled multi-view broadband imagers for ubiquitous sensing platform. *Nat. Commun.* **12**, 3009 (2021).
21. D. Suzuki, K. Li, K. Ishibashi, Y. Kawano, A terahertz video camera patch sheet with an adjustable design based on self-aligned, 2D, suspended sensor array patterning. *Adv. Funct. Mater.* **31**, 2008931 (2021).
22. D. Suzuki, Y. Kawano, Flexible terahertz imaging systems with single-walled carbon nanotube films. *Carbon* **162**, 13–24 (2020).
23. Y. Nonoguchi, M. Nakano, T. Murayama, H. Hagino, S. Hama, K. Miyazaki, R. Matsubara, M. Nakamura, T. Kawai, Simple salt-coordinated n-type nanocarbon materials stable in air. *Adv. Funct. Mater.* **26**, 3021–3028 (2016).
24. T. Araki, Y. Okabe, N. Kurihira, Y. Kasai, T. Noda, T. Sekitani, Low-temperature printable and stretchable circuit board and its application to flexible hybrid electronics, in *2021 International Conference on Electronics Packaging* (IEEE, 2021), pp. 61–62.
25. T. Yamada, Y. Hayamizu, Y. Yamamoto, Y. Yomogida, A. Izadi-Najafabadi, D. N. Futaba, K. Hata, A stretchable carbon nanotube strain sensor for human-motion detection. *Nat. Nanotechnol.* **6**, 296–301 (2011).
26. S. Ryu, P. Lee, J. B. Chou, R. Xu, R. Zhao, A. J. Hart, S. G. Kim, Extremely elastic wearable carbon nanotube fiber strain sensor for monitoring of human motion. *ACS Nano* **9**, 5929–5936 (2015).
27. K. Li, D. Suzuki, Y. Kawano, Series photothermoelectric coupling between two composite materials for a freely attachable broadband imaging sheet. *Adv. Photon. Res.* **2**, 2000095 (2021).
28. J. Sun, Y. Zhu, W. Feng, Q. Ding, H. Qin, Y. Sun, Z. Zhang, X. Li, J. Zhang, X. Li, Y. Shangguan, L. Jin, Passive terahertz imaging detectors based on antenna-coupled high-electron-mobility transistors. *Opt. Express* **28**, 4911–4920 (2020).
29. J. Zhou, M. A. R. Miah, Y. Yu, A. C. Zhang, Z. Zeng, S. Damle, I. A. Niaz, Y. Zhang, Y. H. Lo, Room-temperature long-wave infrared detector with thin double layers of amorphous germanium and amorphous silicon. *Opt. Express* **27**, 37056–37064 (2019).
30. J. B. Wang, W. Li, B. Chu, C. S. Lee, Z. Su, G. Zhang, S. H. Wu, F. Yan, High speed responsive near infrared photodetector focusing on 808nm radiation using hexadecafluoro–copper–phthalocyanine as the acceptor. *Org. Electron.* **12**, 34–38 (2011).
31. R. Bogue, Terahertz imaging: A report on progress. *Sens. Rev.* **29**, 6–12 (2009).
32. D. Suzuki, Y. Ochiai, Y. Nakagawa, Y. Kuwahara, T. Saito, Y. Kawano, Fermi-level-controlled semiconducting-separated carbon nanotube films for flexible terahertz imagers. *ACS Appl. Nano Mater.* **1**, 2469–2475 (2018).
33. X. Gou, H. Xiao, S. Yang, Modeling, experimental study and optimization on low-temperature waste heat thermoelectric generator system. *Appl. Energy* **87**, 3131–3136 (2010).
34. P. Kang, M. C. Wang, P. M. Knapp, S. Nam, Crumpled graphene photodetector with enhanced, strain-tunable, and wavelength-selective photoresponsivity. *Adv. Mater.* **28**, 4639–4645 (2016).

35. C. W. Chinag, G. Haider, W. C. Tan, Y. R. Liou, Y. C. Lai, R. Ravindranath, H. T. Chang, Y. F. Chen, Highly stretchable and sensitive photodetectors based on hybrid graphene and graphene quantum dots. *ACS Appl. Mater. Interfaces* **8**, 466–471 (2016).

36. X. Xu, Y. Zuo, S. Cai, X. Tao, Z. Zhang, X. Zhou, S. He, X. Fang, H. Peng, Three-dimensional helical inorganic thermoelectric generators and photodetectors for stretchable and wearable electronic devices. *J. Mater. Chem. C* **6**, 4866–4872 (2018).

37. P. K. Crane, R. Walker, R. A. Hubbard, G. Li, D. M. Nathan, H. Zheng, S. Haneuse, S. Craft, T. J. Montine, S. E. Kahn, W. McCormick, S. M. McCurry, J. D. Bowen, E. B. Larson, Glucose levels and risk of dementia. *N. Engl. J. Med.* **369**, 540–548 (2013).

38. Z. Li, Y. Zhu, W. Zhang, C. Xu, Y. Pan, Y. Zhao, A low-cost and high sensitive paper-based microfluidic device for rapid detection of glucose in fruit. *Food Anal. Methods* **10**, 666–674 (2017).

39. H. Suto, F. Kataoka, N. Kikuchi, R. O. Knuteson, A. Butz, M. Haun, H. Buijs, K. Shiomi, H. Imai, A. Kuze, Thermal and near-infrared sensor for carbon observation fourier transform spectrometer-2 (TANSO-FTS-2) on the greenhouse gases observing SATellite-2 (GOSAT-2) during its first year in orbit. *Atmos. Meas. Tech.* **14**, 2013–2039 (2021).

40. T. Hamazaki, Y. Kaneko, A. Kuze, K. Kondo, Fourier transform spectrometer for greenhouse gases observing satellite (GOSAT), in *Proc. SPIE 5659 Enabling Sensor and Platform Technologies for Spaceborne Remote Sensing* (SPIE, 2005), pp. 73–80.

41. C. P. Walsh, Remote sensing of atmospheric trace gases by ground-based solar fourier transform infrared spectroscopy, in *Fourier Transforms: New Analytical Approaches and FTIR Strategies*, G. Nikolić, Ed. (InTech, 2011), pp. 459–478.

42. M. Zhou, P. Wang, B. Langerock, C. Vigouroux, C. Hermans, N. Kumps, T. Wang, Y. Yang, D. Ji, L. Ran, J. Zhang, Y. Xuan, H. Chen, F. Posny, V. Duflot, J. M. Metzger, M. D. Mazière, Ground-based Fourier transform infrared (FTIR) O_3 retrievals from the 3040 cm^{-1} spectral range at Xianghe, China. *Atmos. Meas. Tech.* **13**, 5379–5394 (2020).

43. R. Olbrycht, M. Kałuża, Optical gas imaging with uncooled thermal imaging camera—Impact of warm filters and elevated background temperature. *IEEE Trans. Ind. Electron.* **67**, 9824–9832 (2020).

44. J. E. Kim, S. S. Kim, C. Zuo, M. Gao, D. Vak, D. Y. Kim, Humidity-tolerant roll-to-roll fabrication of perovskite solar cells via polymer-additive-assisted hot slot die deposition. *Adv. Funct. Mater.* **29**, 1809194 (2019).

45. Z. Gao, C. Bumgardner, N. Song, Y. Zhang, J. Li, X. Li, Cotton-textile-enabled flexible self-sustaining power packs via roll-to-roll fabrication. *Nat. Commun.* **7**, 11586 (2016).

46. K. Chen, W. Gao, S. Emaminejad, D. Kiriya, H. Ota, H. Y. Y. Nyein, K. Takei, A. Javey, Printed carbon nanotube electronics and sensor systems. *Adv. Mater.* **28**, 4397–4414 (2016).

47. S. Nakata, T. Arie, S. Akita, K. Takei, Wearable, flexible, and multifunctional healthcare device with an ISFET chemical sensor for simultaneous sweat pH and skin temperature monitoring. *ACS Sens.* **2**, 443–448 (2017).

48. V. P. Rachim, W. Chung, Multimodal wrist biosensor for wearable cuff-less blood pressure monitoring system. *Sci. Rep.* **9**, 7947 (2019).

49. F. Larachi, D. Aksenova, B. Yousefi, X. P. V. Maldague, G. Beaudoin, Thermochemical monitoring of brucite carbonation using passive infrared thermography. *Chem. Eng. Process.* **130**, 43–52 (2018).

50. B. R. Cosofret, W. J. Marinelli, T. E. Ustun, C. M. Gittins, M. T. Boies, M. F. Hinds, D. C. Rossi, R. L. Coxe, S. D. Chang, B. D. Green, T. Nakamura, Passive infrared imaging sensor for standoff detection of methane leaks, in *Proc. SPIE 5584 Chemical and Biological Standoff Detection II* (SPIE, 2004);doi.org/10.1117/12.581190.

51. M. Kowalski, Hidden object detection and recognition in passive terahertz and mid-wavelength infrared. *J. Infrared Millim. Terahertz Waves* **40**, 1074–1091 (2019).

52. Y. Cheng, Y. Wang, Y. Niu, Z. Zhao, Concealed object enhancement using multi-polarization information for passive millimeter and terahertz wave security screening. *Opt. Express* **28**, 6350–6366 (2020).

53. D. Suzuki, S. Oda, Y. Kawano, A flexible and wearable terahertz scanner. *Nat. Photon.* **10**, 809–813 (2016).

54. V. Hers, D. Corbugy, I. Joslet, P. Hermant, J. Demarteau, B. Delhougne, G. Vandermoten, J. P. Hermanne, New concept using passive infrared (PIR) technology for a contactless detection of breathing movement: A pilot study involving a cohort of 169 adult patients. *J. Clin. Monit. Comput.* **27**, 521–529 (2013).

55. D. Suzuki, Y. Ochiai, Y. Kawano, Thermal device design for a carbon nanotube terahertz camera. *ACS Omega* **3**, 3540–3547 (2018).

56. V. Giurgiutiu, K. Reifsnider, R. Kriz, B. Ahn, J. Lesko, Influence of fiber coating and interphase on the design of polymeric composite strength—Analytical predictions, in *36th Structures, Structural Dynamics and Materials Conference* (AIAA, 1995);doi.org/10.2514/6.1995-1212.

57. M. Miwa, A. Takeimo, H. Yamazaki, A. Watanabe, Strain rate and temperature dependence of shear properties of epoxy resin. *J. Mater. Sci.* **30**, 1760–1765 (1995).

58. D. J. O'Brien, N. R. Sottos, S. R. White, Cure-dependent viscoelastic Poisson's ratio of epoxy. *Exp. Mech.* **47**, 237–249 (2007).

59. H. J. Qi, M. C. Boyce, Stress–strain behavior of thermoplastic polyurethanes. *Mech. Mater.* **37**, 817–839 (2005).

60. V. Kanyanta, A. Ivankovic, Mechanical characterisation of polyurethane elastomer for biomedical applications. *J. Mech. Behav. Biomed.* **3**, 51–62 (2010).

61. T. Otsuji, Trends in the research of modern terahertz detectors: Plasmon detectors. *IEEE Trans. Terahertz Sci. Technol.* **5**, 1110–1120 (2015).

62. D. Zhang, Y. Song, L. Ping, S. Xu, D. Yang, Y. Wang, Y. Yang, Photo-thermoelectric effect induced electricity in stretchable graphene-polymer nanocomposites for ultrasensitive strain sensing. *Nano Res.* **12**, 2982–2987 (2019).

63. X. He, N. Fujimura, J. M. Lloyd, K. J. Erickson, A. A. Talin, Q. Zhang, W. Gao, Q. Jiang, Y. Kawano, R. H. Hauge, F. Léonard, J. Kono, Carbon nanotube terahertz detector. *Nano Lett.* **14**, 3953–3958 (2014).

64. M. He, Y. J. Lin, C. M. Chiu, W. Yang, B. Zhang, D. Yun, Y. Xie, Z. H. Lin, A flexible photo-thermoelectric nanogenerator based on MoS_2/PU photothermal layer for infrared light harvesting. *Nano Energy* **49**, 588–595 (2018).

65. Y. Zhong, L. Zhang, V. Linseis, B. Qin, W. Chen, L. D. Zhao, H. Zhu, High-quality textured SnSe thin films for self-powered, rapid-response photothermoelectric application. *Nano Energy* **72**, 104742 (2020).

66. W. Wu, Y. Wang, Y. Niu, P. Wang, M. Chen, J. Sun, N. Wang, D. Wu, Z. Zhao, Thermal localization enhanced fast photothermoelectric response in a quasi-one-dimensional flexible NbS_3 photodetector. *ACS Appl. Mater. Interfaces* **12**, 14165–14173 (2020).

67. M. Zhang, J. T. W. Yeow, A flexible, scalable, and self-powered mid-infrared detector based on transparent PEDOT:PSS/graphene composite. *Carbon* **156**, 339–345 (2020).

68. A. Cao, P. L. Dickrell, W. G. Sawyer, M. N. Ghasemi-Nejhad, P. M. Ajayan, Super-compressible foamlike carbon nanotube films. *Science* **25**, 1307–1310 (2005).

69. S. Park, S. Vosguerichian, Z. Bao, A review of fabrication and applications of carbon nanotube film-based flexible electronics. *Nanoscale* **5**, 1727–1752 (2013).

70. S. Kivistö, T. Hakulinen, A. Kaskela, B. Aitchison, D. P. Brown, A. G. Nasibulin, E. I. Kauppinen, A. Härkönen, O. G. Okhotnikov, Carbon nanotube films for ultrafast broadband technology. *Opt. Express* **17**, 2358–2363 (2009).

71. B. A. MacLeod, N. J. Stanton, I. E. Gould, D. Wesenberg, R. Ihly, Z. R. Owczarczyk, K. E. Hurst, C. S. Fewox, C. N. Folmar, K. H. Hughes, B. L. Zink, J. L. Blackburn, A. J. Ferguson, Large n- and p-type thermoelectric power factors from doped semiconducting single-walled carbon nanotube thin films. *Energ. Environ. Sci.* **10**, 2168–2179 (2017).

72. Y. Nakai, K. Hond, K. Yanagi, H. Kataura, T. Kato, Y. Yamamoto, Y. Maniwa, Giant Seebeck coefficient in semiconducting single-wall carbon nanotube film. *Appl. Phys. Express* **7**, 025103 (2014).

73. D. Hayashi, Y. Nakai, H. Kyakuno, T. Yamamoto, Y. Miyata, K. Yanagi, Y. Maniwa, Improvement of thermoelectric performance of single-wall carbon nanotubes by heavy doping: Effect of one-dimensional band multiplicity. *Appl. Phys. Express* **9**, 125103 (2016).

74. A. Kosarev, S. Rumyantsev, M. Moreno, A. Torres, S. Boubanga, W. Knap, Si_xGe_y:H-based micro-bolometers studied in the terahertz frequency range. *Solid State Electron.* **54**, 417–419 (2010).

75. S. A. Kuznetsov, A. G. Paulish, M. Navarro-Cía, A. V. Arzhannikov, Selective pyroelectric detection of millimetre waves using ultra-thin metasurface absorbers. *Sci. Rep.* **6**, 21079 (2016).

76. D. Y. Kim, K. O. Kenneth, Reduction of NEP variations for terahertz detectors using Schottky barrier diodes in CMOS. *Electron. Lett.* **53**, 732–734 (2017).

77. R. Huang, X. Ji, Y. Liao, J. Peng, K. Wang, Y. Xu, F. Yan, Dual-frequency CMOS terahertz detector with silicon-based plasmonic antenna. *Opt. Exp.* **27**, 23250–23261 (2019).

78. S. Suzuki, T. Nukariya, Y. Ueda, T. Otsuka, M. Asada, High current responsivity and wide modulation bandwidth terahertz detector using high-electronmobility transistor for wireless communication. *J. Infrared Millim. Terahertz Waves* **37**, 658–667 (2016).

79. Y. Kurita, G. Ducournau, D. Coquillat, A. Satou, K. Kobayashi, S. B. Tombet, Y. M. Meziani, V. V. Popov, W. Knap, T. Suemitsu, T. Otsuji, Ultrahigh sensitive sub-terahertz detection by InP-based asymmetric dualgrating-gate high-electron-mobility transistors and their broadband characteristics. *Appl. Phys. Lett.* **104**, 251114 (2014).

80. L. Dong, R. Yue, L. Liu, Fabrication and characterization of integrated uncooled infrared sensor arrays using a-Si thin-film transistors as active elements. *J. Microelectromech. Syst.* **14**, 1167–1177 (2005).

81. X. Yang, A. Vorobiev, A. Generalov, M. A. Andersson, J. Stake, A flexible graphene terahertz detector. *Appl. Phys. Lett.* **111**, 021102 (2017).

82. A. Paddubskaya, M. Demidenko, K. Batrakov, G. Valušis, T. Kaplas, Y. Svirko, P. Kuzhir, Tunable perfect THz absorber based on a stretchable ultrathin carbon-polymer bilayer. *Materials* **12**, 143 (2019).

83. T. Q. Trung, V. Q. Dang, H. B. Lee, D. Kim, S. Moon, N. E. Lee, H. Lee, An omnidirectionally stretchable photodetector based on organic—Inorganic heterojunctions. *ACS Appl. Mater. Interfaces* **9**, 35958–35967 (2017).

84. J. Ding, H. Fang, Z. Lian, Q. Lv, J. L. Sun, Q. Yan, High-performance stretchable photodetector based on $CH_3NH_3PbI_3$ microwires and graphene. *Nanoscale* **10**, 10538–10544 (2018).

85. J. Yoo, S. Jeong, S. Kim, J. H. Je, A stretchable nanowire UV–Vis–NIR photodetector with high performance. *Adv. Mater.* **27**, 1712–1717 (2015).

86. M. Kim, P. Kang, J. Leem, S. W. Nam, A stretchable crumpled graphene photodetector with plasmonically enhanced photoresponsivity. *Nanoscale* **9**, 4058–4065 (2017).